Modelling the motion of particles around choanoflagellates

By B. A. A. ORME, J. R. BLAKE AND S. R. OTTO

School of Mathematics and Statistics, The University of Birmingham, Edgbaston,
Birmingham, B15 2TT, UK

The three-dimensional particle paths due to a helical beat pattern of the flagellum of a sessile choanoflagellate, *Salpingoeca Amphoridium* (SA), are modelled and compared to the experimental observations of Pettitt (2001). The organism's main components are a flagellum and a cell body which are situated above a substrate such that the interaction between these entities is crucial in determining the fluid flow around the choanoflagellate. This flow of fluid can be characterized as Stokes flow and a flow field analogous to one created by the flagellum is generated by a distribution of stokeslets and dipoles along a helical curve.

The model describing the flow considers interactions between a slender flagellum, an infinite flat plane (modelling the substrate) and a sphere (modelling the cell body). The use of image systems appropriate to Green's functions for a sphere and plane boundary are described following the method of Higdon (1979*a*). The computations predict particle paths representing passive tracers from experiments and their motion illustrates overall flow patterns. Figures are presented comparing recorded experimental data with numerically generated results for a number of particle paths. The principal results show good qualitative agreement with the main characteristics of flows observed in the experimental study of Pettitt (2001).

1. Introduction

As motivation for the study of filter feeding currents around sessile microscopic organisms, we consider the motion of particles around *Salpingoeca Amphoridium* (SA), a choanoflagellate. This organism belongs to the phylum Protozoa and we investigate this specific organism due to the availability of experimental data provided in Pettitt (2001). The paths taken by particles are important when investigating the optimum feeding patterns of these organisms. The model replicates the main features of the organism along with the associated interactions due to the physical boundaries.

Figure 1(*a*) shows a photograph of SA which can be compared to the sketch in figure 1(*b*). Typically, we can describe SA from the base upwards as consisting of, first, a stalk attached to a substrate (which maybe a rigid surface or one covered in mucus) and joined at the other end to the cell. In the experiments from which we have taken the data, the substrate was a human hair. In some cases, we also find organisms directly attached to the substrate. The flagellum, which emerges from the opposite pole of the cell body causes the fluid to circulate around the organism. A collar made up of fine finger-like projections, called micro-villi, emerges from the cell body and extends upwards and outwards around the flagellum. The collar is the filter where particles may become trapped before being transported close to the base of the
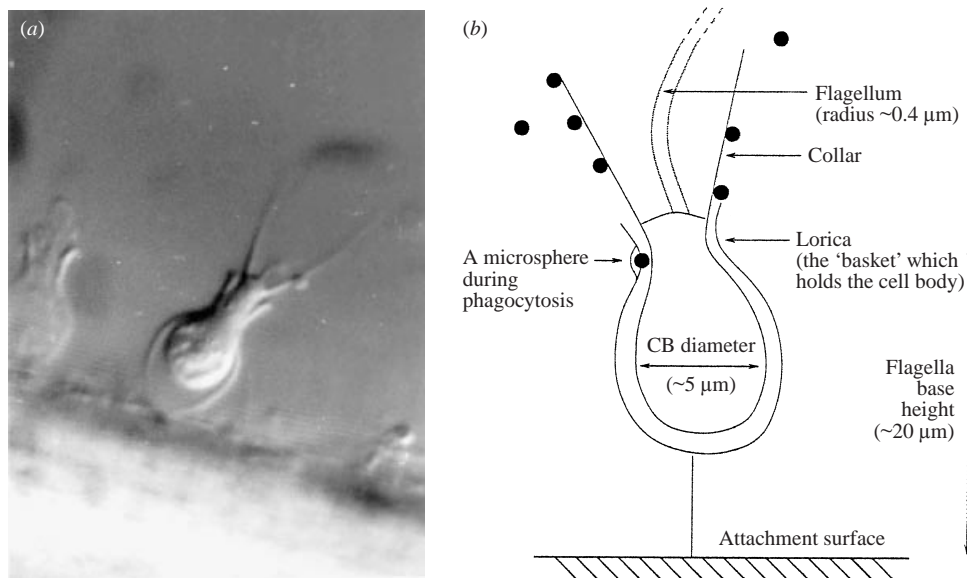
FIGURE 1. (*a*) A photograph and (*b*) an illustration of *Salpingoeca Amphoridium* showing details of the scale and structure. The photograph is magnified approximately 1000 times and the illustration is not to scale. The figure shows details of microspheres in the fluid, attached to the collar and at the base of the collar where one is being engulfed by the cell membrane.

flagellum (i.e. the 'mouth' region) where the particles can be engulfed by phagocytosis. Alternatively, the collar may not retain the intercepted particles, providing another method by which mixing may be increased due to the release back into the fluid of these particles at a later time. This is explored in detail in Shimeta & Jumars (1991) who investigate various particle interception and retention methods.

In experiments, the particle size has been investigated to consider the effect on retention of nutrients by SA. The latex microspheres used by Pettitt (2001) were 0.5 µm in diameter. For the purpose of the model, we consider point particles influenced by the flagellum in the same manner as particles in experiments, to give a perspective on the flow fields. We do not include the stalk's influence in the model because we assume that the effect of the cell body has a much greater influence on the fluid flow than the stalk. As in Higdon (1979*a*), and for simplification, we neglect the addition of the collar at this stage. Due to the relative size of micro-villi compared to the cell and flagellum, this simplification is shown to provide a good initial approximation to the problem. Another simplification is the consideration of just one organism because in nature there generally exists an interaction among many of these organisms. However, by initially considering the model for the case of a single cell and flagellum system, we could infer the types of flow patterns we expect around a system where there is an interaction between more than one organism. Blake, Otto & Blake (1998), Otto, Yannacopoulos & Blake (2001) and Orme, Otto & Blake (2001*a*,*b*) consider various axisymmetric and two-dimensional flow interactions between two displaced forces which can be considered indicative of the way two adjacent organisms may interact, in some cases leading to chaotic mixing.

Typical dimensions of SA are of microscopic length scales implying that the Reynolds number is very small and consequently viscous forces dominate, leading to Stokes flow equations for modelling purposes. For example, the length of the flagellum

is typically $20\,\mu m$ whilst the cell body has diameter $5\,\mu m$, see figure $1(b)$. These length scales together with the environmental factors such as the characteristic speed $(100\,\mu m\,s^{-1})$ and the dynamic viscosity $(10^{-2}\,g\,\mu m^{-1}\,s^{-1})$ imply this quantification of the Reynolds number. References to small Reynolds numbers for a range of problems involving micro-organisms are given in Brennen & Winet (1977).

We extend the method initially given by Higdon (1979a) beyond the range of that work to investigate flow patterns. Lighthill (1976) gives an excellent overview and review of flagellar hydrodynamics, encompassing flagellar motions and flow fields generated by a flagellum; he later revisited the subject, see Lighthill (1996). Higdon (1979a) relies on using the method of distributing singularities along the centreline of the flagellum to model the organism, along with a number of simplifying assumptions. Following this, the appropriate image system satisfying the boundary conditions in an approximate way is developed in greater detail in §2.4. This leads to a complicated set of singularities, see Blake (1971) and Higdon (1979b).

The far-field structure due to the stokeslet and image system near a plane boundary will be shown to be particularly relevant to particle path behaviour. Whilst the helical beat pattern yield vertical and horizontal forces of the same magnitude, the far-field decay of the velocity field for the vertical force is much weaker, being $O(r^{-3})$ compared to that of the horizontal force which is $O(r^{-2})$. Furthermore, the vertical force leads to a toroidal eddy structure whilst the horizontal force yields a stresslet far field with radial streamlines. It will be seen that particles in the far field have a predominantly radial motion superimposed on a loop structure.

The flagellar beat of SA occurs in three dimensions with a helical wave shape, the type of beat used during this study. The first part of §2 formulates the helical beat pattern, extending the planar case in Higdon (1979a). Note that in later work, Higdon (1979c) does consider helical waves but with regard to the propulsion of a motile organism rather than a sessile organism. This initial formulation of the case of the helical wave includes considering the image systems required to satisfy the no-slip boundary conditions on the wall, the cell body and the flagellum.

Section 3 presents results of paths traced by particles in three-dimensional space. By varying the parameters of the problem, we are then able to compare and contrast our results to those observed experimentally by Pettitt (2001). Discussion of the work, including how improvements have been incorporated into previous work, is presented. We finally conclude in §4 with a brief summary and details of possible extensions.

2. Representing and modelling the flow field

By specifying the shape of the flagellum as a function of time, we can determine the velocity induced on particles within the fluid due to the forces created by the flagellum using a distribution of singularities along the centreline. First, the form of the centreline of the curve along which we position stokeslets and dipoles to represent the flow field induced by the beating flagellum is presented. The image system to satisfy conditions on any boundaries within the problem is then constructed leading to an approximate representation of the system.

2.1. *Kinematics*

Introducing a function to represent the flagellum will allow one to determine the boundary conditions which must be satisfied to obtain an approximate solution to the problem in terms of the force generated along the flagellum. The forces distributed along the flagellum vary depending on position and time but for a helical
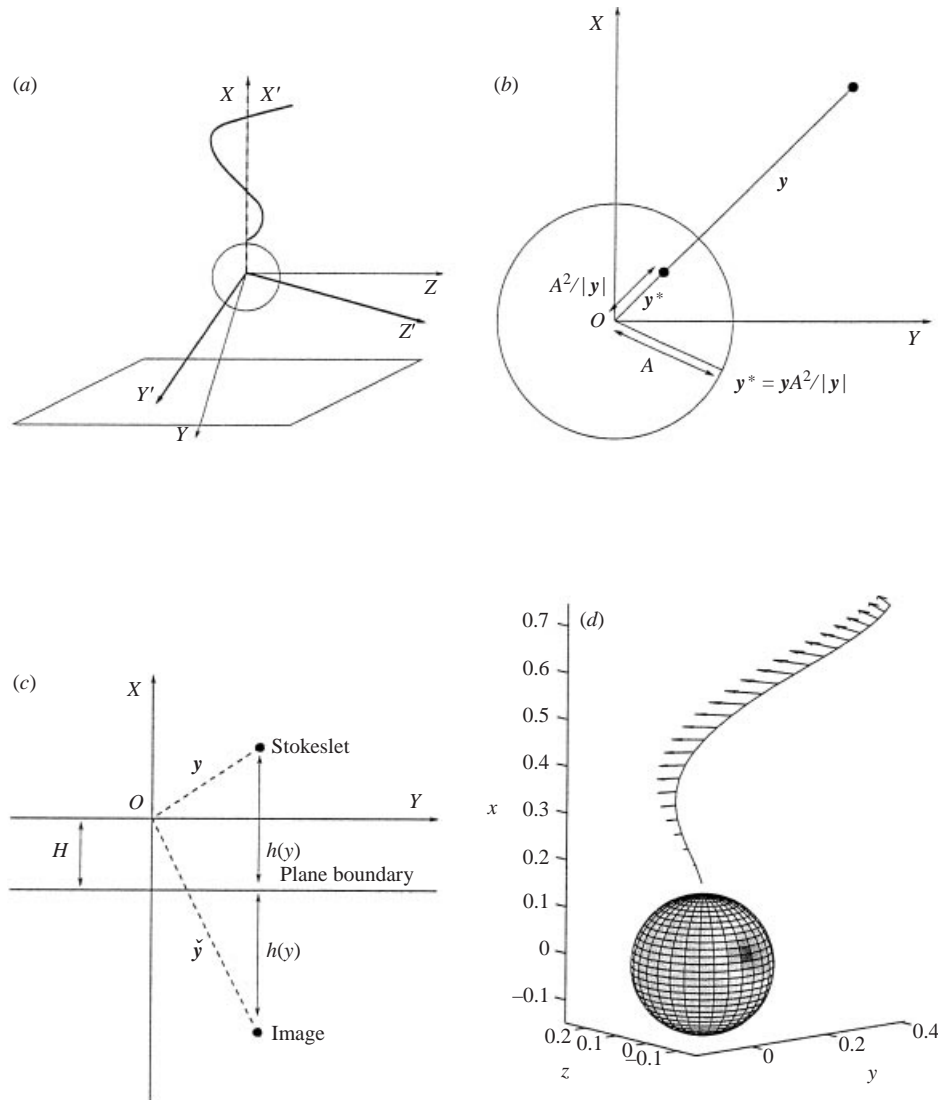
FIGURE 2. Features of the three-dimensional model: (*a*) the rotating coordinate system with the axis of the flagellum coinciding with both the laboratory frame (non-primed coordinates) and the rotating flagellum frame (primed coordinates); (*b*) the inverse point, $\mathbf{y}^*$, in a sphere; (*c*) the image point, $\check{\mathbf{y}}$, in a plane; and (*d*) the velocity components along the centreline of the flagellum, the sphere representing the cell body with diameter 0.2 units, the flagellum of length 1.0 unit whilst the substrate (not shown) is parallel to the (y, z)-plane and cuts the x-axis at 0.9 units below the origin.

wave they will have the same form throughout the beat cycle. This property is exploited to investigate the interaction of the forces with a tracer particle. The forces and hence the velocities created within the fluid around SA can be determined by simply changing the line along which the forces of the flagellum lie. The velocity of any tracer is determined once the position of the flagellum and the location of the associated forces with respect to the tracer are known. Section 2.2 introduces the rotating coordinate system to describe how the flagellum, cell body and substrate boundary conditions change with time.

Figure 2(*a*) (based on figure 1 in Higdon 1979*a* but showing rotating axes) shows the model we use to describe the coordinate axes relative to the helical wave pattern, cell body and substrate in three-dimensional space. We can define a wave form as in Higdon (1979*a*), such that

$$Y(X,t) = E(X - X_0)\alpha \sin[k(X - X_0) - \omega t], \\ Z(X,t) = E(X - X_0)\alpha \cos[k(X - X_0) - \omega t], \Big\} \tag{2.1}$$

where $X = (X, Y(X,t), Z(X,t))$ describes any point along the flagellum and X_0 is the X-coordinate giving the height of the base of the flagellum. The wave speed is $c = \omega/k$ in the positive x-direction, where ω is the radian frequency and k the wavenumber. The parameter α describes the amplitude of the wave, which grows gradually from the base and reaches its maximum about a third of the way along its length. Incorporating the exponential function $E(x) = 1 - \exp(-(k_E x)^2)$ into expressions (2.1) gives a realistic waveform. In this case, $k_E = 5$ gives $E(x) \approx 0.9$ when $x = 0.3$. This function also satisfies the condition that the flagellum is attached radially to the cell body with radius A, i.e. $E(0) = E'(0) = 0$.

For consistency, we assume the flagellum is inextensible. We will divide the flagellum into segments of equal length, in this case using arc length as the length dimension. The beginning and the end of each segment are denoted by s_i and s_{i+1} respectively, where $i = 0, \ldots, N - 1$ and the flagellum is split into N intervals. The arc length is given by the usual formula

$$s = \int_{X_0}^{X} \left[1 + \left(\frac{\partial Y}{\partial X} \right)^2 + \left(\frac{\partial Z}{\partial X} \right)^2 \right]^{1/2} dX. \tag{2.2}$$

Each of the N segments has length L/N, where the total length of the flagellum is L. Substituting into equation (2.2) the known values of each s_i (for $i = 1, \ldots, N$) we can determine the corresponding X-coordinates and thence, from (2.1) the Y- and Z-coordinates. (Notice that s_i can be described as giving the arc length from the base of the flagellum to the end of the ith interval). This is calculated via interpolation which allows one to accurately find the corresponding value of X for a known value of s.

We now have a vector describing the motion of a particular segment of the flagellum for each time step and for each arc length position (s_i). We assume the flagellum is approximated using linear segments, and the midpoint of each segment, s_i^m, can be defined to lie equidistant between each s_i and s_{i+1} along the centreline of the flagellum. These coordinates are used to enable the derivation of the forces created by the singularities which are taken to be situated at the midpoint of each flagellum segment. Hancock (1953) describes the method we use to place a distribution of stokeslets and dipoles along the centreline of the flagellum. By assuming that the flagellum can be described as slender, i.e. as having a small radius compared to its length, one can find the velocity induced at any segment on the flagellum. Therefore, Hancock (1953) has shown that by assuming the length of a segment ($|s_{i+1} - s_i|$) to be large compared to the flagellum radius, the consideration of a distribution of singularities within a segment making a contribution to the velocity of the segment is a sufficiently good representation of the forces. Since this process can be repeated for all segments, we can build up the velocity profile created by the entire flagellum.

2.2. *Particle paths – fixed and rotating coordinate frames*

We study two coordinate axes, a rotating frame and a laboratory frame, whose origins and vertical axes are coincident and fixed, illustrated by figure 2(*a*). The rotating frame

is taken to be fixed with respect to the flagellum and the coordinates of general points in this frame are given by X'. The laboratory frame, with coordinates labelled as X, is fixed with respect to the cell body and the plane. Therefore, within the laboratory frame, the flagellum appears to be rotating about the vertical axis with an angular velocity ω. Moving between the two reference frames requires a transformation matrix defined by

$$
T(\omega t) = \begin{pmatrix} 1 & 0 & 0 \\ 0 & \cos\omega t & -\sin\omega t \\ 0 & \sin\omega t & \cos\omega t \end{pmatrix} \quad \text{with} \quad X' = T(\omega t)X,
$$

giving the coordinates in the rotating frame from the known coordinates of the laboratory frame. The transformation back from the rotating to the body frame simply replaces ωt with $-\omega t$ in the matrix T. One must initially calculate the particle positions within the rotating frame because this is the frame in which the force is evaluated. These points can then be translated to the laboratory frame to obtain a picture of the trajectory as observed in the experimental studies of Pettitt (2001).

Translation from the laboratory to the rotating frame will take the form $X' = T(\omega t)X$, where X' can then be acted upon by the velocity field due to the flagellum. We assume X' moves to $X' + \delta X'$ under the action of this force. This is the new position in the rotating system which is needed to translate back to the laboratory frame. If the frame has moved through an angle ωt since the start of the motion, then $X_{\mathrm{NEW}} = T(-\omega t)[X' + \delta X']$ gives the new position of the particle in the laboratory frame. From here, we use the particle position with respect to the laboratory frame to construct the particle trajectory. We finally must find the position of the particle within the rotating frame which has moved through a further angle of $\omega\,\delta t$. Hence repeating the translation back to the rotating frame gives $X'_{\mathrm{NEW}} = T(\omega(t + \delta t))X_{\mathrm{NEW}}$. This final translation step is a subtle difference, but shows how one cannot simply consider the effect the force has on the points within the rotating frame alone due to the small rotation of the flagellum frame.

As well as examining the rotating axes, it is important to consider the boundary conditions of the problem. We must always solve the same physical system, even if the relative geometry used to describe the problem has changed. We represent the velocities as

$$
V_F = V_B - \omega \times X,
$$

where V_F is the velocity in the rotating flagellum frame, and V_B is the velocity in the laboratory frame. This yields the boundary conditions on the cell body and plane in the flagellum frame to be of a non-zero velocity whilst the flagellum will have zero velocity. This is implemented by equation (2.25) in §2.6.

2.3. *The singularity structure*

This section gives details of each of the singularities and image systems needed to find an approximate representation of the flow fields around SA. For simplicity, we initially present results for the fixed coordinate system but move to the rotating coordinate system presented in §2.2 once all the principles of the physical problem are defined.

Higdon (1979*a*) modelled an organism which he assumed had a smooth slender flagellum and a spherical cell body, with the height of the cell body a fixed distance above the substrate. The flagellum was represented by placing stokeslets and dipoles

along its centreline. Because the flagellum is attached to a cell body above a substrate, the interaction between these separate entities (the sphere and the plane) needs to be taken into account. Green's functions, in terms of singularities and image systems, are used to allow the boundary conditions to be satisfied approximately to second order.

We consider a very thin flagellum where we take its length, L, to be much greater than the flagellum radius, a (i.e. $L \gg a$) and the centreline to be a helical wave (2.1). Along this line, we distribute both stokeslets and dipoles with their associated image systems. Due to the approximations of a slender body, the image system and the distribution of singularities, Higdon (1979a) is able to state that this model is representative of the effects of the flagellum within this system. Following the progression of particles over time around the model of a single organism will lead to insight into how well mixed the particles can become and allows comparison with the experimental results in Pettitt (2001). Interesting comparisons to the flow fields created in the axisymmetric case where a single point force creates an approximate representation of the flagellum could also be made (Orme *et al.* 2001a,b). In previous axisymmetric work, where there are two dimensions of space and the third dimension is time, chaos can be studied due to the action of two alternating stokeslets (Blake *et al.* 1998; Otto *et al.* 2001).

The problem, defined by Higdon (1979a), initially requires the use of a stokeslet, a Stokes-doublet and a dipole, which give the fundamental building blocks for the model. For all of these singularities, we regard the force to be acting at a point $\boldsymbol{y}$ whilst the tracer which the force is affecting is situated at $\boldsymbol{x}$, i.e. $\boldsymbol{y}$ is a location of the singularity on the centreline of the flagellum, whilst $\boldsymbol{x}$ is the general position of a particle within the fluid. The stokeslet is given by

$$S_{jk}(\boldsymbol{x}, \boldsymbol{y}) = \frac{\delta_{jk}}{r} + \frac{r_j r_k}{r^3}, \tag{2.3}$$

where we define $r = |\boldsymbol{x} - \boldsymbol{y}|$ and $r_m = (x_m - y_m)$. This definition is carried throughout the following work, along with δ_{jk} which is the Kronecker delta function. This stokeslet creates a velocity at $\boldsymbol{x}$, due to a force with strength and direction $\boldsymbol{f}$ acting at $\boldsymbol{y}$, defined by

$$u_j(\boldsymbol{x}) = S_{jk}(\boldsymbol{x}, \boldsymbol{y}) f_k / 8\pi\mu.$$

Here, the parameter μ represents the viscosity of the fluid. The subscripts j or k (as for all the following work) indicate the components of the force, $\boldsymbol{f}$, or the velocity, $\boldsymbol{u}$, with respect to direction.

The second type of singularity, a Stokes-doublet, can be derived by using the operator $\partial/\partial y_l$ on equation (2.3); due to linearity this gives another solution to the Stokes equations:

$$S_{jkl}^D(\boldsymbol{x}, \boldsymbol{y}) = \left(-\frac{\delta_{kl}}{r^3} + \frac{3r_k r_l}{r^5} \right) r_j + \left(\frac{r_l \delta_{jk} - r_k \delta_{jl}}{r^3} \right). \tag{2.4}$$

If the Stokes-doublet has tensoral strength σ_{kl}, then the velocity at the point $\boldsymbol{x}$ due to a Stokes-doublet acting at point $\boldsymbol{y}$ is given by

$$u_j(\boldsymbol{x}) = S_{jkl}^D(\boldsymbol{x}, \boldsymbol{y}) \sigma_{kl} / 8\pi\mu.$$

Physically, the Stokes-doublet consists of two components. From equation (2.4), the first is the symmetric component called a stresslet, representing the straining motion of the fluid. The second is the antisymmetric component called a rotlet. Physically, this generates a flow due to the action of a torque.

Finally, we operate on equation (2.3) with respect to $-\frac{1}{2}\nabla_y^2 = -\frac{1}{2}\partial^2/\partial y_k^2$ to find the dipole, given by

$$D_{jk}(\boldsymbol{x},\boldsymbol{y}) = \frac{-\delta_{jk}}{r^3} + \frac{3r_jr_k}{r^5}, \tag{2.5}$$

which has the same tensoral structure as the stokeslet and is critical to the development of slender body theory, Lighthill (1976). Again, the velocity field $\boldsymbol{u}$ at a point $\boldsymbol{x}$ created by a dipole of strength and direction $\boldsymbol{d}$ which is situated at $\boldsymbol{y}$, is

$$u_j(\boldsymbol{x}) = D_{jk}(\boldsymbol{x},\boldsymbol{y})\,d_k/4\pi.$$

Equations (2.3), (2.4) and (2.5) give all the components we require to be able to construct the Green's function enabling the description of the fluid flow around the flagellum, cell body and substrate whilst satisfying the relevant boundary conditions by the introduction of image systems.

2.4. *Construction of the image systems*

As mentioned at the start of §2.3, the distribution of singularities along the flagellum creates a velocity field which alone does not satisfy all the boundary conditions of the problem to a satisfactory degree of accuracy. By the introduction of specific Green's functions, which include the image systems for these singularities, the correct combination of singularities can be considered such that we satisfy all the given boundary conditions to second order with respect to the radius of the cell body over the distance from the plane. Once we have satisfied the no-slip conditions on the plane boundary (i.e. the substrate) we need to consider how the introduction of the image singularities have affected the other boundary conditions, such as the no-slip condition on the sphere (i.e. the cell body). Hence, we simultaneously have to consider the sphere's surface, and the sphere and boundary interaction. We present first the image system for a sphere, second that for a plane and finally combine the two, enabling all the boundary conditions to be satisfied approximately to second order, as above.

The Green's function for flow external to a sphere is

$$G_{jk}^S(\boldsymbol{x},\boldsymbol{y}) = S_{jk}(\boldsymbol{x},\boldsymbol{y}) + S_{jk}^*(\boldsymbol{x},\boldsymbol{y}), \tag{2.6}$$

where S_{jk}^* represents the image system located within the sphere. The velocity at any point $\boldsymbol{x}$ due to a point force $\boldsymbol{f}$ acting at a point $\boldsymbol{y}$ in the presence of a sphere is thus

$$u_j(\boldsymbol{x}) = G_{jk}^S(\boldsymbol{x},\boldsymbol{y})f_k/8\pi\mu. \tag{2.7}$$

The components of this equation have the same definitions as those given after equation (2.3). The expression for S_{jk}^* is a lengthy algebraic one and details can be found in Appendix A and Higdon (1979*a*). However, physically it is informative to consider how the expression is constructed with regard to the forces acting within the system. The image system involves considering singularities associated with the inverse point $\boldsymbol{y}^*$ defined as

$$\boldsymbol{y}^* = \frac{A^2}{|\boldsymbol{y}|^2}\boldsymbol{y} = \frac{A^2}{|\boldsymbol{y}|}\left(\frac{\boldsymbol{y}}{|\boldsymbol{y}|}\right),$$

which is the image in the sphere of the point $\boldsymbol{y}$. In this problem, the origin and the centre of the sphere are coincident, see figure 2(*b*). Higdon (1979*a*) gives S_{jk}^* in

terms of y^* as derived by Oseen (1927) along with a simpler expression in terms of individual fundamental singularities. As an approximation to the Oseen expression for the image system, one can consider the first- and second-order terms in an expansion of the expression for the image system about the origin, when the radius of the sphere is much smaller than the distance of the stokeslet from the origin, i.e. $A \ll |y|$. The physical construction of this image system can be explained in terms of the radial and transverse components of the stokeslet. Radially, the images of a stokeslet are: a stokeslet, a dipole and a stresslet all situated at the inverse point. Transversely, the images are: line distributions of stokeslets, dipoles and Stokes-doublets which stretch from the origin to the inverse point. By neglecting terms $O(A^2/|y|^2)$ which are very small, Higdon (1979a) gives an expression for S_{jk}^* which lends itself to numerical methods better than Oseen's complicated expression.

Now that we have an expression for the image of a stokeslet, $S_{jk}^*(x, y)$, we can use the following rule to enable one to find images of the higher-order singularities, such as the image of the Stokes-doublet and the dipole, which are also required to enable the boundary conditions to be satisfied. This rule specifies that if we have a solution of the Stokes equations defined by a certain differentiable operator, then the image system in the sphere for this solution (singularity) is defined by the same differential of the image of the solution.

The strength of the distribution of stokeslets along the flagellum, which we will calculate in §2.6, and their interaction with the sphere, enable the calculation of the force and couple acting on the sphere, therefore giving the flow fields generated by the flagellum. The interaction of the introduced singularities must also be considered as they too will have image systems due to the interaction between the flagellum, plane and sphere. These image systems will therefore affect the calculation of the force and moment on the sphere as well as the flow fields. Hence, using the rule defined above, the images of a Stokes-doublet and a dipole in the sphere are given by

$$\partial(S_{jk}^*)/\partial y_l = S_{jkl}^{D*}(x, y), \quad -\nabla_y^2(S_{jk}^*)/2 = D_{jk}^*(x, y).$$

A concise and complete set of sphere images are available and the explicit versions can be found in both Appendix A and Higdon (1979a) who decomposes each image system into its simpler first- and second-order terms as previously explained for the image system of the stokeslet.

The image system for a plane requires image singularities at the image point $\check{y}$. Defining p to be a unit vector perpendicular to the plane (the substrate in this case) and pointing in the direction of the fluid (upwards for an organism situated above the substrate) then we can define $\check{y}$ as in figure 2(c) by

$$\check{y} = y - 2h(y)p, \tag{2.8}$$

where $h(y)$ is the distance of the point y from the substrate. The Green's function for the half-space, G_{jk}^P, is

$$G_{jk}^P(x, y) = S_{jk}(x, y) + \check{S}_{jk}(x, y), \tag{2.9}$$

where $\check{S}_{jk}$ is the image system for the plane and consists of a stokeslet, a Stokes-doublet and a dipole, all situated at the image point $\check{y}$ (with $\check{S}_{jk}$ given explicitly in Appendix B).

In the case of the image system for the plane, we have no difficulty in expressing the terms for the image system in the plane. However, in the case of the sphere it was necessary to distribute the singularities such that there were each of a stokeslet,

a dipole and a stresslet all situated at the inverse point as well as a line distribution of stokeslets, dipoles and Stokes-doublets from the origin to the inverse point. This ensured that both radial and transverse components of the boundary condition on the sphere were satisfied. In the case of the plane, there is no such distribution of singularities owing to the simpler geometry of a plane compared to a sphere and so the resulting image system is more apparent.

Higdon (1979a) makes an initial conjecture (a first approximation) that the Green's function must be composed of the stokeslet along with both the image systems for the plane and the sphere, i.e. the combined image system, to represent the physical system. This gives

$$G_{jk}(x, y) \approx S_{jk}(x, y) + S^*_{jk}(x, y) + \check{S}_{jk}(x, y). \tag{2.10}$$

However, we also have the problem of considering the images of the other singularities which are present in equation (2.10), i.e. the contribution from the terms S^*_{jk} and $\check{S}_{jk}$, and the effects their combined force distributions induce on the boundary conditions. Although the individual image systems for the sphere and plane may satisfy the boundary conditions independently, the combined effect induced by their images does not. Therefore, we need to consider the image of the plane's image system ($\check{S}_{jk}$) in the sphere, denoted by $\check{S}^*_{jk}$. Again the reason for its form is easily understood by examining a breakdown of the terms included in $\check{S}^*_{jk}$ (see Appendix B). Briefly, the image system for the plane consists of a stokeslet, a Stokes-doublet and a dipole, and so by replacing all of these singularities by their images in the sphere, we have found the images of the plane image system in the sphere. Appending equation (2.10), the next degree of approximation for the combined Green's function is

$$G_{jk}(x, y) \approx S_{jk}(x, y) + S^*_{jk}(x, y) + \check{S}_{jk}(x, y) + \check{S}^*_{jk}(x, y). \tag{2.11}$$

This expression still does not satisfy the boundary conditions to second order within our model. For an improved approximation we will need to consider terms from both S^*_{jk} and $\check{S}_{jk}$ whose plane images are not in (2.11).

This process is broken into three stages to enable all the boundary conditions to be satisfied by determining which singularities are violating which specific boundary conditions. First, the leading-order terms of the plane images for the terms S^*_{jk} and $\check{S}_{jk}$ are considered. We replace the stokeslets of these leading-order terms,

$$-3\{AS_{kl}(0, y)S_{jl}(x, 0) + A\check{S}_{kl}(0, y)S_{jl}(x, 0)\}/4,$$

by their plane images

$$-3\{AS_{kl}(0, y)\check{S}_{jl}(x, 0) + A\check{S}_{kl}(0, y)\check{S}_{jl}(x, 0)\}/4. \tag{2.12}$$

However, in adding equation (2.12) to equation (2.11) and correcting the velocity on the plane, we have induced another velocity on the sphere's surface. We minimize this velocity in an attempt to satisfy the boundary conditions by adding the sphere image given in (2.12) to equation (2.11). Expression (2.12) can be rewritten to satisfy this condition as

$$-3\{AS_{kl}(0, y)\check{S}^*_{jl}(x, 0) + A\check{S}_{kl}(0, y)\check{S}^*_{jl}(x, 0)\}/4. \tag{2.13}$$

Hence, adding both (2.12) and (2.13) to equation (2.11), we have satisfied the boundary conditions on the plane and sphere to second order.

The final Green's function when considering the flow due to a force acting at y in the presence of a sphere within the half-plane above a plane boundary is

$$G_{jk}(x, y) = S_{jk}(x, y) + S_{jk}^*(x, y) + \check{S}_{jk}(x, y) + \check{S}_{jk}^*(x, y)$$
$$-3\{A[S_{kl}(0, y) + \check{S}_{kl}(0, y)][\check{S}_{jl}(x, 0) + \check{S}_{jl}^*(x, 0)]\}/4, \qquad (2.14)$$

where again the velocity created at x due to the system described is

$$u_j(x) = G_{jk}(x, y)f_k/8\pi\mu.$$

This velocity is due to the contribution of only a single force at position y which we assume to lie at some location along the centreline of the flagellum. Section 2.5 considers the effects of many of these forces distributed along a curve defining the centreline of the flagellum. This enables the velocity at any position x to resemble velocities created within a flow field around any organism similar to that which we have chosen to model.

2.5. *Flow fields associated with singularities representing the flagellum*

The velocity induced by the whole flagellum may be represented in terms of the following integral by (the currently unknown) force and dipole distribution along the central axis of the flagellum:

$$u_j(x) = \int_0^L \left[G_{jk}(x, X(s))\frac{f_k(s)}{8\pi\mu} + D_{jk}(x, X(s))\frac{d_k(s)}{4\pi} \right] ds. \qquad (2.15)$$

The expression for the velocity on the left-hand side of equation (2.15) can be obtained from the boundary conditions, which for the flagellum can be determined from partially differentiating equation (2.1) with respect to time, t, to give

$$u = \frac{\partial X}{\partial t} = \left(\frac{\partial X}{\partial t}, \frac{\partial Y}{\partial t} + \frac{\partial Y}{\partial X}\frac{\partial X}{\partial t}, \frac{\partial Z}{\partial t} + \frac{\partial Z}{\partial X}\frac{\partial X}{\partial t} \right). \qquad (2.16)$$

The differential terms are calculated from equation (2.1) by simply differentiating the equation defining the flagellum centreline. The term $\partial X/\partial t$ requires more involved calculations in most cases but in the case of a circular cylindrical helical wave, $\partial X/\partial t \equiv 0$.

A relation between the forces created by the stokeslets and the dipoles can be exploited in the computations. Higdon (1979*a*) stated that the dipole strength was determined by the component of the stokeslet normal to the centreline:

$$d_k = \frac{-a^2}{4\mu}(\delta_{kl} - T_k T_l)f_l, \qquad (2.17)$$

where T is defined as the unit tangent vector to the flagellum. Therefore, we rewrite equation (2.15) so that it only contains one unknown, i.e. $f_k(s_i)$ which gives the force on the ith segment of the flagellum in the kth direction. A detailed explanation is given in Lighthill (1996) for how this relationship is derived from to the distribution of stokeslets and dipoles along the centreline of the flagellum.

2.6. *Solving to find the force, f*

First, rewrite equation (2.15) so that the right-hand side is in terms of known expressions for the singularities introduced in §2.3 and the forces $f_k(s)$. This will allow numerical calculation and manipulation to determine the unknown forces $f_k(s_i)$ for each position s_i along the flagellum in equation (2.15).

The boundary condition on the flagellum allows the evaluation of the left-hand side of equation (2.15), i.e. the velocity of the fluid on the flagellum surface equals the velocity of the flagellum surface. We consider this boundary condition at points along the centreline instead of at the surface because the distribution of stokeslets and dipoles is along the flagellum centreline. The Green's functions need both the coordinates where forces distributed along the flagellum act and the coordinates of the point at which we are interested in recording the effects of the force. Dividing the flagellum into 'segments', typically linear with end points at s_i and s_{i+1}, the force on each of them acting at the midpoint, s_i^m can be calculated.

Defining S_{jk}^{ϕ} as the sum of the image terms in equation (2.14), we can use the definition given in Higdon (1979a) to re-express the relation involving the Green's function as

$$S_{jk}^{\phi}(\boldsymbol{x}, \boldsymbol{y}) = G_{jk}(\boldsymbol{x}, \boldsymbol{y}) - S_{jk}(\boldsymbol{x}, \boldsymbol{y}), \tag{2.18}$$

separating the image terms (from equation (2.14)) into those which require numerical integration (terms from expressions (A 1), (B 1) and (B 2)) and the remaining terms which can be analytically integrated. In our case, separation of the terms helps to break the numerical problem down into discrete components. Each of the terms in equation (2.18) has been interpreted in the preceding sections, making it easier to evaluate for a large number of variables.

To numerically integrate (2.15) we begin by rewriting it using (2.18) as

$$u_j(\boldsymbol{x}) = \int_0^L \left\{ [S_{jk}(\boldsymbol{x}, \boldsymbol{X}(s)) + S_{jk}^{\phi}(\boldsymbol{x}, \boldsymbol{X}(s))] \frac{f_k(s)}{8\pi\mu} + D_{jk}(\boldsymbol{x}, \boldsymbol{X}(s)) \frac{d_k(s)}{4\pi} \right\} \mathrm{d}s. \tag{2.19}$$

Following Higdon (1979a), the flagellum length is divided into N equal segments and within each we assume the force of the stokeslet, $\boldsymbol{f}$, is constant. To find the force for any given time will require incorporating the details of the rotating system into the boundary conditions. We relate the forces created due to the singularities (f_k) and those due to the dipoles (d_k) via equation (2.17), reducing the problem to solving for f_k alone. For the term S_{jk}^{ϕ} given in equation (2.18), we consider any nth interval and more specifically the integral over a small length segment given by

$$H_{jk}(\boldsymbol{x}, \boldsymbol{X}(s_n)) = \frac{1}{8\pi\mu} \int_{s_n^m - \delta s_n}^{s_n^m + \delta s_n} S_{jk}^{\phi}(\boldsymbol{x}, \boldsymbol{X}(s)) \, \mathrm{d}s; \tag{2.20}$$

this integration needs to be evaluated numerically. The length of the segment is $2\delta s_n$, which is taken to be small. Evaluating the induced velocity when considering the N intervals requires a summation over all N segments along the total length of the flagellum for all the terms H_{jk}, plus the other terms into which equation (2.19) is decomposed. Hence we choose to express the remainder of equation (2.19) in terms of the nth interval, allowing this summation over the N segments to give the value of the velocity. We define K_{jk} as

$$K_{jk} = \frac{1}{8\pi\mu} \int_{s_n^m - \delta s_n}^{s_n^m + \delta s_n} \left\{ S_{jk}(\boldsymbol{x}, \boldsymbol{X}(s)) - \frac{a^2}{2} (\delta_{kl} - T_l T_k) D_{jl}(\boldsymbol{x}, \boldsymbol{X}(s)) \right\} \mathrm{d}s, \tag{2.21}$$

thus allowing one to write a simple equation re-expressing equation (2.19) as the summation

$$u_j(\boldsymbol{x}) = \sum_{n=1}^{N} \{ [K_{jk}(\boldsymbol{x}, \boldsymbol{X}(s_n)) + H_{jk}(\boldsymbol{x}, \boldsymbol{X}(s_n))] f_k(s_n) \}, \tag{2.22}$$

with f_k the unknown force to be determined. Care needs to be taken at both the proximal and distal ends of the flagellum to avoid singularities (see for example Gueron & Levit-Gurevich 2001a,b; Gueron & Liron 1992). We note that at the proximal end the flagellum shape and motion are carefully chosen. At the distal end, the cross-sectional shape can be chosen to allow the singularity distribution to terminate before the end of the flagellum.

Expression (2.17) gives a simplified method with which to consider the force distribution. Its validity is due to considering the force on a small interval whose effects become negligible compared to the rest of the forces along the flagellum (Hancock 1953). The numerical expression (2.22) gives the velocity induced by the singularity distributions along the flagellum, including the images in both the plane and the sphere. The final stage to determine the values of f_k is to substitute for the boundary conditions on the flagellum so that one can evaluate the Green's functions and the flagellum velocity. The numerical scheme can then be implemented where there exists only one unknown set of variables, f_k. Using matrix inversion from MatLab software, rather than an iteration method as in Higdon (1979a), we calculate the values of f_k acting at the midpoint of each segment along the flagellum. The midpoint, for any qth interval, is denoted as $X(s_q^m)$ within the Cartesian coordinate system. Hence, equation (2.22) satisfies the boundary conditions on the flagellum in the physical system when

$$u_j(X(s_q^m)) = \sum_{n=1}^{N} \{[K_{jk}(X(s_q^m), X(s_n)) + H_{jk}(X(s_q^m), X(s_n))]f_k(s_n)\}. \qquad (2.23)$$

Since the velocity of the flagellum centreline is given by equation (2.16) when $X = X(s_q^m)$, this must also give the left-hand side of equation (2.23) by the definition of the no-slip boundary condition. The terms on the right-hand side of (2.23) are easily calculated because we can express the Green's functions numerically for any coordinates $X(s_q^m)$ from the singularities and image system expressions previously defined. It is helpful to express the elements within the summation term as

$$Q_{jk}(s_q^m, s_n) = K_{jk}(X(s_q^m), X(s_n)) + H_{jk}(X(s_q^m), X(s_n)), \qquad (2.24)$$

which we refer to later when we investigate the solution via matrix inversion. However, this is computationally expensive and is much simpler to undertake in a rotating frame involving just one solution of equation (2.19). This yields a fixed helix and a rotating spherical body and plane boundary. Thus the velocity boundary conditions now yield no-slip on the flagellum and rigid body rotation on the sphere and plane boundary. We can simply alter equation (2.23) to satisfy the boundary conditions within the rotating frame, giving

$$u_j(X(s_q^m)) = \sum_{n=1}^{N} \{[K_{jk}(X(s_q^m), X(s_n)) + H_{jk}(X(s_q^m), X(s_n))]f_k(s_n)\} - (\boldsymbol{\omega} \times X(s_q^m))_j, \qquad (2.25)$$

which can be solved once by a simple matrix inversion to find the forces along the flagellum in the rotating frame.

The remaining work involves rearranging equation (2.25) so that we can determine the unknown values of the forces created by the flagellum. Representing the force and the velocity at the given points along the flagellum by two vectors, the summation term given in equation (2.25) can be represented as a matrix which can therefore be inverted. Hence for each time step, once we have calculated the right-hand side of
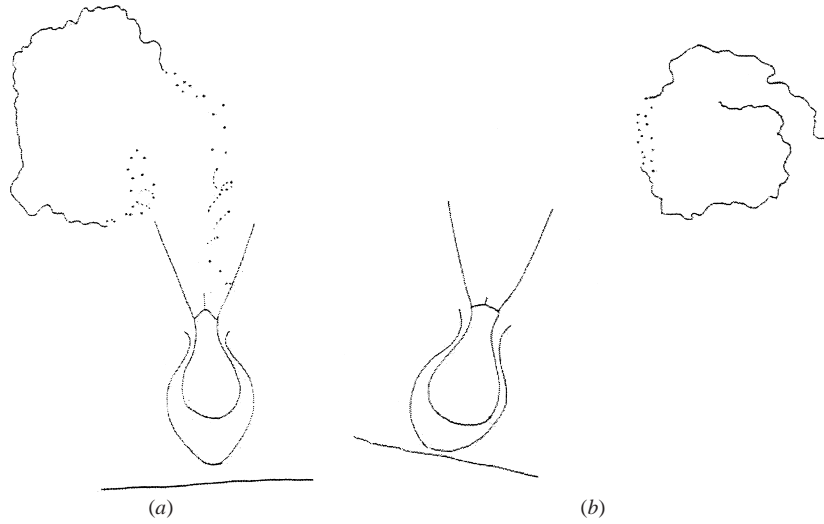
FIGURE 3. The outline of two specific SA (organisms (*a*) A and (*b*) C in table 1) and specific particle paths taken from experimental observations. Both illustrate the eddy structure whilst (*a*) also indicates the near-field 'loopiness'.

equation (2.25) and then inverted the matrix which we call **Q**, from equation (2.24), we can determine the value of *f* by simple matrix multiplication.

When the force is known, we can solve equation (2.22) for any given point within the system because all the terms on the right-hand side can be calculated. The particle position is calculated at each time step using an Eulerian scheme:

$$x_{\text{new}} = x_{\text{old}} + v(x_{\text{old}})\delta t, \tag{2.26}$$

where $v(x)$ is the velocity at position x given by equation (2.22). This Eulerian formulation will require the calculation of the velocity at each specific time. The values for the initial point, x_{old}, and the time step δt which are used in (2.26) are either stated in the initial conditions of the model, or in the case of x_{old}, known from the preceding calculation. The value of the time step δt has been varied to assure the fidelity of the results and the value used in the main corresponds to one fifth of 0.02 s as recorded from the experimental data (Pettitt 2001). Repeating this process allows one to trace a particle's position over many periods of the beat by recording x_{new} over any length of time in the rotating frame. A simple translation back to the laboratory frame with each time step reproduces the corresponding physical system.

3. Results and discussion

This section will illustrate some of the qualitative similarities between the numerical calculations of particle paths and experimental results found in Pettitt (2001). First, we present results concerning the action of the flagellum and then look at a number of paths a tracer particle follows for a variety of different sets of parameters.

Figure 2(*d*) illustrates the velocity on the surface of the flagellum at a nominal time during a period of the beat. It is the forces created along the flagellum which ultimately affect any particle or tracer within the flow. By studying figures similar to figure 2(*d*) and examining the magnitude of the velocity at points along the flagellum, we know that the magnitude will remain the same throughout the problem, the velocity only changing in direction due to the propagation of the helical wave of the flagellum.

	Non-dim. control	A (μm)	Non-dim.	B (μm)	Non-dim.	C (μm)	Non-dim.
Flagellum radius	0.01	0.4	0.02	0.4	0.03	0.4	0.01
Cell body radius	0.1	2.5	0.13	2.4	0.15	2.5	0.17
Flagellum length	1	19.2	1	15.8	1	11.4	1
Height above substrate	0.9	11.4	0.46	8.8	0.56	6.4	0.22

TABLE 1. Dimensions of SA as taken from experimental results by Pettitt (2001) for one control and three living organisms with a variety of physically different parameters. For each organism (A, B and C) we show the dimensions in μm and the non-dimensionalized lengths in the adjacent column.

We investigate a representation of particle paths which will allow constructive comparison of numerical results with experimental results. For both results, there are a number of cases we choose to consider, each relevant to a different species or size of choanoflagellate (as represented in table 1). We show how the numerics replicate the key characteristics of the flow patterns recorded in experimental observations via some representative figures. The comparisons of path lines will be dependent on the dimensions of the relevant organism and so we consider a number of parameters. Note that the effect of the collar is not present within these calculations, but one could consider its virtual situation within the fluid. This would enable one to obtain results about the interception of tracers with the collar along similar lines to the study of Berg & Purcell (1977).

We present illustrations taken from experimental recordings and numerical interpretations of particle paths. Figure 3 shows two traces from a video of an experiment which observed a number of SA feeding, corresponding to organism A and C whose dimensions are included in table 1. The particle paths are traced by polystyrene spheres which have been introduced into the flow. The positions of these tracers are recorded at a given time increment. The position of the specific choanoflagellate which creates the flows is also included. This type of recording gives a two-dimensional representation within a given depth of focus (approximately 5 μm) of what is in fact a three-dimensional process. The flagellum or particles can therefore move out of the field of focus as is clearly evident for the flagella in figure 3 which are out of focus. This will mean the loss of some accuracy from the results when we compare these video images with those generated from our numerical model which are obviously fully three-dimensional. For this reason, figure 4, which illustrates the results of the numerically generated particle paths, shows two different perspectives. Figure 4(*a*) gives a fully three-dimensional representation so that the flagellum shape and cell body are clearly seen. Figure 4(*b*) shows a slice of the three-dimensional space where the depth of the slice is approximately twice the cell body diameter. This is shown as a plane representation, similar to the view one would see down a microscope and comparable to figure 3.

We now consider in more detail the numerical representations of particle paths (figures 4 and 5) for the specific dimensions of the organisms labelled 'control' and 'C' in table 1. Altogether there are three cases motivated by experimental results (columns two to seven in table 1) and one set of control parameters which was used purely for numerical methods (column one in table 1). Comparing the four columns all showing non-dimensionalized results for SA (given by the heading 'Non-dim.' in
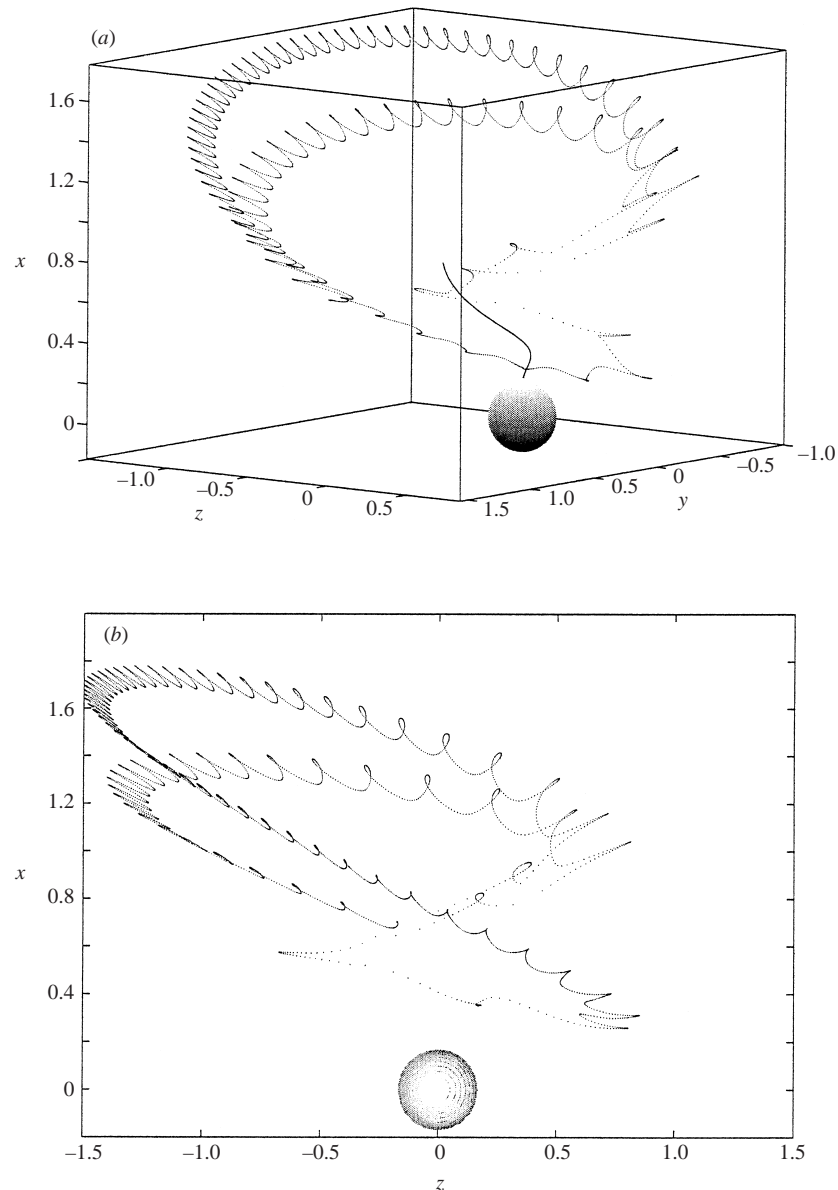
FIGURE 4. Graphics generated to show the recirculation of tracers seen within the fluid, for organism C whose dimensions are given in table 1. (*a*) The paths followed by a particle around the cell body and the flagellum. This is over long time and shows the total three-dimensional representation including the eddies followed by the tracer. (*b*) A two-dimensional projection of the three-dimensional numerics onto a plane. This creates an image similar to the representation recorded from experimental observations.

table 1), one can see the first control test set is representative of the case where the cell body is positioned approximately one flagellum length from the substrate. The other three cases look at a range of parameters where the substrate distance from the flagellum is smaller than the associated flagellum lengths.

We have taken measurements from figure 3(*b*) to compare with the paths generated by numerical methods (presented in figure 4) involving an organism modelled with

	Experimental		Numerical		
	Eddy width	Eddy length	Eddy width	Eddy length	Distance of eddy from flagellum base
Org. A	0.11	0.07	0.25	0.64	1.07
Org. B	0.15	0.11	0.21	0.21	2.17
Org. C	0.26	0.37	0.31	0.54	0.74

TABLE 2. Measurements of specific eddies created around three organisms whose flow patterns we investigate, non-dimensionalized with respect to H^*, the distance between the substrate and flagellum base, to allow comparison between experimental and numerical results. Width and length are interchangeable and merely suggest measurements taken in two mutually perpendicular directions. The distance of the eddy from the flagellum base is the same for both sets of results to facilitate comparisons of the correct eddy measurements.

the same dimensions. It is unrealistic to compare these results by observations alone to see whether features from the numerical simulation of particle paths agree with those found in experimental results. Therefore, we take measurements of the size of the eddies created, their location and the behaviour of particles from a number of different regions around the organism. By investigating trajectories which are started in accordance with experimental results one creates a basis for numerical procedures when beginning to generate realistic particle paths. The measurements given in table 2 show how we start to look at comparisons between experimental and numerical results. We have included measurements for various organisms (presented in table 1) but only include figures for organism C. The measurements are in non-dimensionalized form with respect to the distance from the substrate to the base of the flagellum, H^*. We use H^* because this distance can be easily measured from the experimental records and is readily available from the numerics. We have found agreement between size and position of eddies created by our numerical model and experimental observations. Referring to both figure 4 and table 2, notice how the eddies (the zig-zag patterns created as the particle moves) from the numerical results are all slightly larger than those found experimentally. This could be due to the affects of a greater viscosity of fluid, the presence of the collar within the physical system which retards the motion of the particles or Brownian motion.

The collar may well influence motion near the cell. However it is splayed out radially so that the gap between the collar filaments is many radii wide at the distal end (Pettitt 2001). At the proximal end little flow occurs because of the no-slip condition on the cell. Over one beat the mean migration due to Brownian motion of the most commonly used particles (0.5 μm) is approximately 0.5–1.0 radii yielding an experimentally observable jiggling motion in the far-field motion. In terms of the Péclet number its magnitude will vary from $O(10^3)$ near the flagellum to $O(1)$ in the far field. Nevertheless Brownian motion may lead to enhanced mixing as noted in the earlier study by Otto *et al.* (2001). However Brownian motion will be random whereas the particle movement attributed to the flagellum will be deterministic with characteristic 'looping' behaviour.

The experimental results are captured at time steps imposed by the type of recording apparatus used. This shows fewer steps between each particle movement so that the tracer appears to jump between one line and another. With the numerics however,
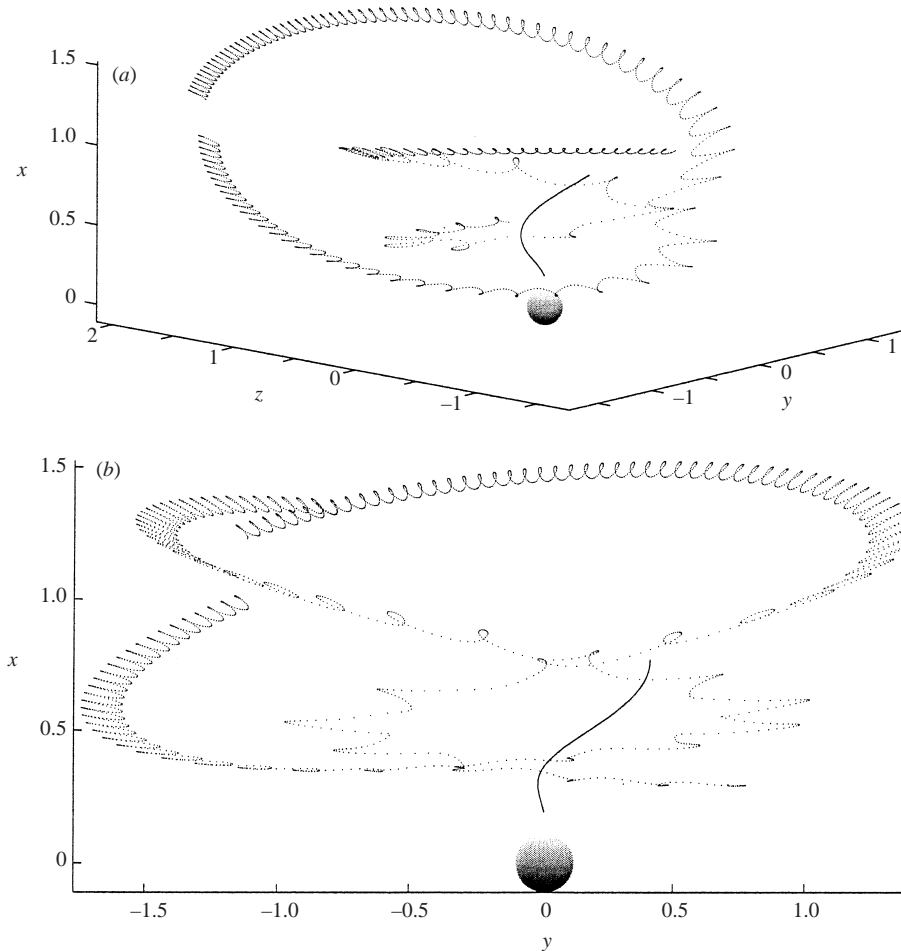
FIGURE 5. The numerical trajectory of particles over time illustrating the recirculation of tracers seen within the fluid. A representation of a scaled sphere and flagellum is given for completeness. For this particular case, the parameters used are for the control organism in table 1. The substrate would be situated 0.9 units below the origin for both figures. (*a*) The paths followed by two particles around the cell body and the flagellum. Notice the eddies creating a continuous recirculation of particles and the larger velocities close to the flagellum. (*b*) A view along the z-axis at a projection of onto a two-dimensional plane. The eddies are now clearer. We see an elongation of the eddies radially; note that the axes are equal.

the smaller time steps used allow a more complete picture in which the particles move in a continuous manner. For example, to recreate the experimental recordings close to the flagellum, we would only be required to sample the particle position every fifth time step from the numerical results.

We have also considered the larger eddies (responsible for recirculating fluid) which consist of many of the smaller eddies whose typical dimensions are displayed in table 2. Again, eddies created via numerical methods are of a similar size and dimension to those from the experimental observations but would appear to be more helical than planar in structure. This may suggest a more elliptical path for the helix than a circular one as used here. These large eddies create the mixing which is of most interested from a biological viewpoint. They show the manner in which these

		X	Y	Z
Near	$y = 0.1$	0.0111	0.0133	0.0161
Middle	$y = 0.35$	0.0074	0.0416	0.0325
Far	$y = 1.0$	0.0114	0.0159	0.0080

TABLE 3. The average displacement in all three coordinate directions (X, Y, Z) of the trajectories of two particles with initial positions given by $(0.75, y, 0)$ and $(0.76, y + 0.01, 0)$ where y varies depending on the region, as given in the table. The trajectory is recorded over ten periods of the flagellar beat.
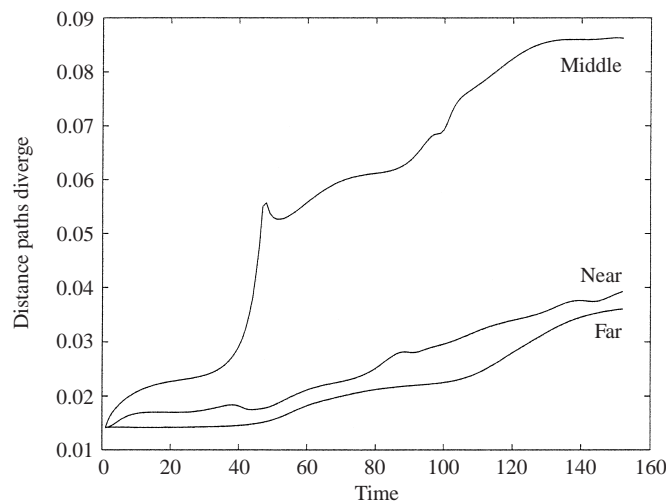
FIGURE 6. The distances by which two trajectories diverge for the three regions (near, middle and far) around the organism. The horizontal axis gives the non-dimensional time whilst the vertical axis shows the distance two particle paths diverge. Table 3 gives details of the initial location and separation of the particles.

organisms circulate fluid to obtain a supply of nutrients from the otherwise stationary fluid. Referring to figure 5 one can see a numerical representation of these larger eddies obtained after several periods of the flagellum beat. Notice how the eddies formed tend to be elongated in the radial direction due to the stresslet far field. However, closer to the flagellum we see a marked vertical progression because of the net vertical force.

It is also interesting to investigate the amount of spreading from various regions by a method which looks at a number of points clustered a given distance from the flagellum and compare the divergence of the trajectories within each such region. We typically take two starting points separated by the distance of one flagellum radius (taken as small) in two of the three coordinate directions. The particles are allowed to move through ten periods of the flagellum beat cycle before we investigate their divergence from one another. The three regions we study around organism C are defined in table 3 and occur at approximately the same vertical position as the flagellum tip; they horizontally are positioned in what may be called the near, middle and far fields. Table 3 gives the average separation of these trajectories calculated by the general mean, along with details of their initial positions relating to the three regions described. Figure 6 shows how the magnitude of the separation of trajectories

changes over ten periods of the beat. This reinforces data from table 3 because we can see that particles typically situated within the mid-field around the flagellum diverge to a greater extent horizontally than vertically. This suggests that particles from this region are most likely to experience more mixing than if they began in either the near or far fields. This does not mean that particles in the near field will not experience significant motion. It merely shows that the trajectories of particles within the near field do not significantly diverge from one another. This could be due to the larger forces created near to the flagellum which do not allow the particles to deviate from a similar path line to their neighbours. In the opposite sense, the far field will not be so significantly affected by the flagellum. Therefore, particles here only move a small distance and will not have the ability to diverge from their neighbours. We refer to Blake (1971) where the image system for a stokeslet in a no-slip boundary was discussed. Results showed how the velocity and force fields are $O(r^{-2})$ for horizontal forces and $O(r^{-3})$ for forces in the vertical direction. Thus we would expect much stronger radial than vertical eddying motion, which is evident from the particle paths, see figure 5. Indeed, the 'loops' show features of a stresslet far field associated with the horizontal forces whereas the vertical forces are observed to have a weaker far-field eddy-generating effect.

Earlier studies using a very idealized model of micro-organism feeding and mixing (Blake *et al.* 1998; Otto *et al.* 2001; Orme *et al.* 2001*a,b*) showed how chaotic mixing can facilitate filtration of nearby liquid. This study also suggests that the characteristic eddy structure allows filtration of the liquid in the intermediate region surrounding the organism. The size of the intermediate region increases with the height of the flagellum above the wall, which in the case of chaonoflagellates is facilitated by the presence of the stalk. Pettitt *et al.* (2002) considered the role of the stalk in three different organisms. This uses a simplified hydrodynamic model by representing the flagellum as a line distribution of stokeslets consistent with the dimensions of the organism and analysing the resultant toroidal eddy shape; findings are broadly in agreement with observation.

4. Conclusions

We have presented a method using Green's functions to allow particle paths around a model organism to be generated. The model is a simplified representation of the substrate, cell body and flagellum of a choanoflagellate by the use of a number of singularities along with their associated image systems. The collar is neglected (and the stalk is only present in a virtual sense) but this is believed to be a good model to represent the flow fields around such an organism.

The use of numerics in this work will allow further investigations to be undertaken by biologists or mathematicians. By generating particle paths found numerically for a certain set of length scales which describe the problem, one could compare these to experimental observations to find estimates of the unknown cell body radius, flagellum length or height above the substrate. The work presented also gives a basis for a mathematical model which could include the collar of the organism. This would increase the accuracy of the results and may enable the numerics to represent the experiments to an even greater degree of accuracy.

We have shown that our results provide a valuable qualitative understanding of the experimental observations, therefore allowing the numerics to act as a tool for a variety of further investigations or studies. For example, the region where the collar will be situated is seen to have a greater level of mixing than the far field. Influencing

mixing of particles is highly beneficial biologically as previous work of Blake *et al.* (1998) has suggested. These results also compare well with theoretical work by Blake (1971) and Higdon (1979*a*).

Appendix A. Singularity expressions as components of the image systems

The image systems are composed of a set of singularities which were stated in Higdon (1979*a*). The expression given in Oseen (1927) for the image system of a stokeslet is difficult to manipulate due to its dependence on the coordinate y, but considering an expansion of the expression about the origin for $A \ll |y|$ leads to simpler expressions. Since we can find the images of the Stokes-doublet and dipole by differentiating the expression for the image of a stokeslet (by the rule stated in §2.4), it is sensible to look for an easily differentiable form of the image system for the stokeslet, S_{jk}^*.

The expansion given in Higdon (1979*a*) for the image system of a stokeslet is composed of the first-order and the second-order terms of the expansion about the origin. The second-order terms are divided into symmetric and antisymmetric components which are denoted by the superscripts $\mathscr{S}$ and $\mathscr{A}$ respectively in this appendix. Denoting the first-order terms by W and the second-order symmetric and antisymmetric terms by $W^{\mathscr{S}}$ and $W^{\mathscr{A}}$, we write the expansion for the image of the stokeslet as

$$S_{jk}^*(x, y) = \left(\frac{\delta_{km}}{|y|} + \frac{y_k y_m}{|y|^3} \right) W_{jm}(x) + \left(\frac{y_k y_m y_n}{|y|^5} \right) W_{jmn}^{\mathscr{S}}(x) + \left(\frac{y_m}{|y|^3} \right) W_{jkm}^{\mathscr{A}}(x), \quad \text{(A 1)}$$

where

$$W_{jk}(x) = -\tfrac{3}{4} A \left(\frac{\delta_{jk}}{|x|} + \frac{x_j x_k}{|x|^3} \right) + \tfrac{1}{4} A^3 \left(-\frac{\delta_{jk}}{|x|^3} + \frac{3 x_j x_k}{|x|^5} \right),$$

$$W_{jkl}^{\mathscr{S}}(x) = -\tfrac{5}{2} A^3 \left(-\frac{x_j \delta_{kl}}{|x|^3} + \frac{3 x_j x_k x_l}{|x|^5} \right) + \tfrac{3}{2} A^5 \left(-\frac{x_j \delta_{kl} + x_k \delta_{jl} + x_l \delta_{jk}}{|x|^5} + \frac{5 x_j x_k x_l}{|x|^7} \right),$$

$$W_{jkl}^{\mathscr{A}}(x) = A^3 \left(\frac{-\delta_{jk} x_l + \delta_{jl} x_k}{|x|^3} \right).$$

We can differentiate equation (A 1) to obtain the images of the higher-order singularities. Because a Stokes-doublet can be derived from differentiating the stokeslet with respect to y_l, then the image of a Stokes-doublet is derived from differentiating equation (A 1) with respect to y_l. This gives

$$S_{jk}^{D*}(x, y) = - \left[\left(-\frac{y_m \delta_{kl}}{|y|^3} + \frac{3 y_k y_l y_m}{|y|^5} \right) + \left(\frac{y_l \delta_{km} - y_k \delta_{lm}}{|y|^3} \right) \right] W_{jm}(x)$$

$$- \left[-\frac{\delta_{kl} y_m y_n + \delta_{lm} y_k y_n + \delta_{ln} y_k y_m}{|y|^5} + \frac{5 y_k y_l y_m y_n}{|y|^7} \right] W_{jmn}^{\mathscr{S}}(x)$$

$$- \left[\frac{\delta_{lm}}{|y|^3} + \frac{3 y_l y_m}{|y|^5} \right] W_{jkm}^{\mathscr{A}}(x). \quad \text{(A 2)}$$

Similarly, the image system for the dipole is found by differentiating once again the image system for the stokeslet (as described in §2.4), to give

$$D_{jk}^*(\boldsymbol{x}, \boldsymbol{y}) = \left[-\frac{\delta_{km}}{|\boldsymbol{y}|^3} + \frac{3 y_k y_m}{|\boldsymbol{y}|^5} \right] W_{jm}(\boldsymbol{x})$$

$$+ \left[-\frac{\delta_{km} y_n + \delta_{kn} y_m + \delta_{mn} y_k}{|\boldsymbol{y}|^5} + \frac{5 y_k y_m y_n}{|\boldsymbol{y}|^7} \right] W_{jmn}^{\mathscr{S}}(\boldsymbol{x}). \qquad \text{(A 3)}$$

Equations (A 1), (A 2) and (A 3) explicitly give the sphere images needed throughout the problem and referred to in §2.4.

Appendix B. Singularity expressions from the combined image system

The combined image system consists of a number of previously defined expressions which include the image system for the plane ($\check{S}_{jk}$) and the image system which is developed from the image of the plane in the sphere ($\check{S}_{jk}^*$). Both these expressions are explicitly stated below in equations (B 1) and (B 2) respectively.

The image system for the plane is constructed from a stokeslet, a Stokes-doublet and a dipole, all considered at the image point in the plane, $\check{\boldsymbol{y}}$, defined in equation (2.8). The total image system for the plane is given by

$$\check{S}_{jk} = -S_{jk}(\boldsymbol{x}, \check{\boldsymbol{y}}) + 2h(\boldsymbol{y}) p_l [\delta_{km} - p_k p_m] S_{jlm}^D(\boldsymbol{x}, \check{\boldsymbol{y}}) - 2h^2(\boldsymbol{y}) [\delta_{km} - p_k p_m] D_{jm}(\boldsymbol{x}, \check{\boldsymbol{y}}). \quad \text{(B 1)}$$

Finally, the most complicated expression we need is for the sphere images of the plane image system, the latter given as $\check{S}_{jk}$ in equation (B 1). We need to use this in equation (2.10) as a constituent of the first approximation to the Green's function for the whole system. We need to consider evaluation of the stokeslet, Stokes doublet and dipole terms within the plane image system at the image point, $\check{\boldsymbol{y}}$. Hence, we take the image system for the plane ($\check{S}_{jk}$), and evaluate it at the image point in the sphere. We define the sphere image of the plane image system as

$$\check{S}_{jk}^* = -S_{jk}^*(\boldsymbol{x}, \check{\boldsymbol{y}}) + 2h(\check{\boldsymbol{y}}) p_l [\delta_{km} - p_k p_m] S_{jlm}^{D*}(\boldsymbol{x}, \check{\boldsymbol{y}}) - 2h^2(\boldsymbol{y}) [\delta_{km} - p_k p_m] D_{jm}^*(\boldsymbol{x}, \check{\boldsymbol{y}}), \quad \text{(B 2)}$$

which contains the same terms as equation (B 1), i.e. the stokeslet, Stokes-doublet and dipole respectively, evaluated at the image point in the sphere (denoted by *).

REFERENCES

BERG, H. C. & PURCELL, E. M. 1977 Physics of chemoreception. *Biophys. J.* **20**, 193–219.

BLAKE, J. R. 1971 A note on the image system for a stokeslet in a no-slip boundary. *Proc. Camb. Phil. Soc.* **70**, 303–310.

BLAKE, J. R., OTTO, S. R. & BLAKE, D. A. 1998 Filter feeding, chaotic filtration and a blinking stokeslet. *Theor. Comput. Fluid Dyn.* **10**, 23–36.

BRENNEN, C. & WINET, H. 1977 Fluid mechanics of propulsion by cilia and flagella. *Annu. Rev. Fluid Mech.* **9**, 339–398.

GUERON, S. & LEVIT-GUREVICH, K. 2001*a* The three dimensional motion of slender filaments. *Math. Meth. Appl. Sci.* **24**, 1577–1603.

GUERON, S. & LEVIT-GUREVICH, K. 2001*b* A three dimensional model for ciliary motions based on internal 9 + 2 structures. *Proc. R. Soc. Lond.* B **268**, 599–607.

GUERON, S. & LIRON, N. 1992 Ciliary motion modelling and dynamic multi cilia interactions. *Biophys. J.* **63**, 1045–1058.

HANCOCK, G. J. 1953 The self propulsion of microorganisms through liquids. *Proc. R. Soc. Lond.* A **217**, 96–121.

HIGDON, J. J. L. 1979*a* The generation of feeding currents by flagellar motions. *J. Fluid Mech.* **94**, 305–330.

HIGDON, J. J. L. 1979*b* A hydrodynamic analysis of flagellar propulsion. *J. Fluid Mech.* **90**, 685–711.

HIGDON, J. J. L. 1979*c* The hydrodynamics of flagellar propulsion: helical waves. *J. Fluid Mech.* **94**, 331–351.

LIGHTHILL, J. 1976 Flagellar hydrodynamics. *SIAM Rev.* **18**, 161–230.

LIGHTHILL, J. 1996 Helical distributions of stokeslets. *J. Engng Maths* **30**, 35–78.

ORME, B. A. A., OTTO, S. R. & BLAKE, J. R. 2001*a* Enhanced efficiency of feeding and mixing due to chaotic flow patterns around choanoflagellates *IMA J. Math. Appl. Medicine Biol.* **18**, 293–325.

ORME, B. A. A., OTTO, S. R. & BLAKE, J. R. 2001*b* Chaos and mixing in microbiological fluid dynamics: Blinking Stokeslets. *Math. Meth. Appl. Sci.* **24**, 1337–1349.

OSEEN, C. W. 1927 *Neuere Methoden und Ergbnisse in der Hydrodynamik*. Leipzig: Akad.-Verlag.

OTTO, S. R., YANNACOPOULOS, A. N. & BLAKE, J. R. 2001 Transport and mixing in Stokes flow: the effect of chaotic dynamics on the blinking stokeslet. *J. Fluid Mech.* **430**, 1–26.

PETTITT, M. 2001 Prey capture and ingestion in choanoflagellates. PhD thesis, Birmingham University.

PETTITT, M., ORME, B. A. A., BLAKE, J. R. & LEADBEATER, B. S. C. 2002 The hydrodynamics of filter feeding in choanoflagellates. *Eur. J. Protistology* **38** (in press).

SHIMETA, J. & JUMARS, P. A. 1991 Physical mechanisms and rates of particle capture by suspension feeders. *Oceanogr. Mar. Biol. Annu. Rev.* **29**, 191–257.